

Neural Network-Based Tensor Model for Nematic Liquid Crystals with Accurate Microscopic Information

Baoming Shi¹, Apala Majumdar², and Lei Zhang^{3*}

¹*School of Mathematical Sciences, Peking University, Beijing 100871, China.*

²*Department of Mathematics and Statistics, University of Strathclyde, G1 1XQ, UK.*

³*Beijing International Center for Mathematical Research, Center for Quantitative Biology, Center for Machine Learning Research, Peking University, Beijing 100871, China.*

The phenomenological Landau-de Gennes (LdG) model is a powerful continuum theory to describe the macroscopic state of nematic liquid crystals. However, it is invariably less accurate and less physically informed than the molecular-level models due to the lack of physical meaning of the parameters. We propose a neural network-based tensor (NN-Tensor) model for nematic liquid crystals, supervised by the molecular model. Consequently, the NN-Tensor model not only attains energy precision comparable to the molecular model but also accurately captures the Isotropic-Nematic phase transition, which the LdG model cannot achieve. The NN-Tensor model is further embedded in another neural network to predict liquid crystal configurations in a domain-free and mesh-free manner. We apply the NN-Tensor model to nematic liquid crystals in a number of two-dimensional and three-dimensional domains to demonstrate it can efficiently identify rich liquid crystal configurations in both regular and non-regular confinements.

Nematic liquid crystals (NLCs) are classical mesophases that combine fluidity with long-range orientational order, but have no positional order [1]. The NLC molecules tend to align along certain locally preferred directions referred to as nematic “directors” in the literature. Consequently, NLCs have anisotropic or direction-dependent physical, optical and rheological properties [2, 3], making them the working material of choice for electro-optic devices, photonics, actuators, elastomers and with tremendous potential in biophysics, nanotechnologies and healthcare technologies [4–6].

There are several mathematical theories for NLCs, ranging from detailed atomistic models, molecular models to fully macroscopic models [1, 7, 8]. The molecular models are characterized by a probability distribution function for the molecular orientations, known as the orientation distribution function (ODF) and intermolecular interaction kernels that contain information about molecular shapes, sizes and interactions [9–12]. However, molecular models suffer from the curse of high dimensionality. On the other hand, macroscopic models are phenomenological and computationally efficient, with fewer degrees of freedom. In particular, the celebrated Landau-de Gennes (LdG) theory has been widely used for modelling two-dimensional (2D) and three-dimensional (3D) liquid crystal equilibria [13–17]. The LdG model describes the macroscopic NLC state by a \mathbf{Q} -tensor order parameter, which contains information about the nematic directors and the degree of orientational ordering within its eigenvectors and eigenvalues respectively. However, the LdG free energy is phenomenological, that is, the precise physical meaning of the LdG parameters are not relatable to molecular-level quantities. The LdG theory is strictly speaking, only valid near the Isotropic-

Nematic (I-N) phase transition temperature, and does not satisfy physical constraints at low temperatures [18].

A more physically informed macroscopic model would be derived from the molecular models [18–20]. One can approximate the ODF by its second moment, \mathbf{Q} , and the corresponding energy can be written in terms of \mathbf{Q} . This procedure has been applied to nematic phase and other LC phases with complex molecular shapes [21]. However, this procedure often results in complex functionals with implicit-dependence on \mathbf{Q} , making them computationally unwieldy and perhaps of interest only in one-dimensional settings [19, 20]. The quasi-entropy method in [22] combines molecular-level information with an explicit \mathbf{Q} -dependence, although it does not achieve molecular-level precisions. The trade-off between computational efficiency and accuracy has been a major dilemma in computational liquid crystal physics.

Recent deep learning advances are capable of bridging the gap between accuracy and computational efficiency. For instance, Behler-Parrinello neural network [23] and deep potential [24, 25] use deep neural networks to build molecular dynamics supervised by first-principle in order to achieve the accuracy of quantum mechanics.

In this letter, we propose a computationally flexible neural network-based tensor (NN-Tensor) model, which employs the microscopic molecular model to guide a new trained bulk energy density for NLCs. Consequently, the NN-Tensor model not only accurately captures the Isotropic-Nematic phase transition but also preserves energy precision comparable to the molecular model, which the LdG model cannot achieve. The NN-Tensor model is further embedded in another neural network to efficiently compute liquid crystal configurations in a domain-free and mesh-free manner.

In the molecular model, the order parameter is the ODF, $f(\mathbf{m})$, which measures the probability of finding molecules with orientation $\mathbf{m} \in \mathbf{S}^2$ [26]. For example,

* Contact author: zhangl@math.pku.edu.cn

the Maier-Saupe (M-S) energy [27] is given by:

$$E_M(f) = \tau \int_{\mathbf{S}^2} f(\mathbf{m}) \ln f(\mathbf{m}) d\mathbf{m} + \frac{\kappa}{2} \int_{\mathbf{S}^2} \int_{\mathbf{S}^2} \left(\frac{1}{3} - (\mathbf{m} \cdot \hat{\mathbf{m}})^2 \right) f(\mathbf{m}) f(\hat{\mathbf{m}}) d\mathbf{m} d\hat{\mathbf{m}}. \quad (1)$$

The first term, $\tau E_{entropy}(f)$, is the entropy energy with a positive τ . τ is proportional to the absolute temperature. The second term, $\kappa E_{potential}(f)$, is the potential energy induced by M-S two-body interactions and $\kappa > 0$ measures the strength of the intermolecular interactions. We set $\tau = 1$ in (1) and adjust the functional with the parameter κ , so that κ is inversely proportional to the absolute temperature. The computational domain is $\Omega \times \mathbf{S}^2$ for inhomogeneous problems, which is two dimensions higher than Ω and hence, the curse of high dimensionality.

The second moment of f ,

$$\mathbf{Q}(x) = \int_{\mathbf{S}^2} \left(\mathbf{m} \times \mathbf{m} - \frac{\mathbf{I}_3}{3} \right) f(\mathbf{x}, \mathbf{m}) d\mathbf{m}, \quad (2)$$

is often used as a measure of the orientational ordering. It is a traceless 3×3 matrix by definition, so that $\mathbf{Q} = 0$ for the uniform ODF without any special or distinguished directions. From the spectral decomposition theorem, we have that $\mathbf{Q} = \sum_{i=1}^3 \lambda_i \mathbf{n}_i \times \mathbf{n}_i$, where $\{\mathbf{n}_1, \mathbf{n}_2, \mathbf{n}_3\}$ are the eigenvectors and $\lambda_1 \leq \lambda_2 \leq \lambda_3$ are the associated eigenvalues respectively, subject to $\sum_{i=1}^3 \lambda_i = 0$. Further, the eigenvalues are naturally constrained to be

$$-\frac{1}{3} < \lambda_i = \int_{\mathbf{S}^2} (\mathbf{m} \cdot \mathbf{n}_i)^2 f(\mathbf{x}, \mathbf{m}) d\mathbf{m} - \frac{1}{3} < \frac{2}{3}. \quad (3)$$

by the second moment definition of \mathbf{Q} in (2). A \mathbf{Q} is deemed admissible in the molecular framework if and only if $\lambda_i \in (-\frac{1}{3}, \frac{2}{3})$ for $i = 1, 2, 3$.

We work in a variational framework and a viable free energy, $E(\mathbf{Q})$, must contain at least two competing contributions: a bulk energy, $E_b(\mathbf{Q})$, which dictates the preferred NLC phase in spatially homogeneous samples, and the elastic energy, $E_{elastic}(\mathbf{Q}, \nabla \mathbf{Q})$, which penalizes spatial inhomogeneities [1]. The free energy must also respect frame indifference and material symmetry properties i.e., for any $\mathbf{P} \in SO(3)$,

$$E_b(\mathbf{PQP}^T) = E_b(\mathbf{Q}). \quad (4)$$

The famous LdG energy, $E_{LdG}(\mathbf{Q}_M)$ is a simple and typical free energy that meets these requirements [1], where \mathbf{Q}_M is the LdG tensor order parameter. However, \mathbf{Q}_M is independent of the ODF and is not compatible with the inequalities (3). Moreover, the LdG bulk energy, $E_b(\mathbf{Q}_M)$, is a quartic polynomial or a truncated expansion near the isotropic state, $\mathbf{Q}_M = 0$, whose coefficients do not have a clear molecular interpretation. Hence, it is not surprising that LdG predictions can fail for low temperatures or near defects and critical phenomena.

NN-Tensor model—Our key idea is to use neural networks to map a given \mathbf{Q} to an ODF, and then to the

M-S energy (1). For brevity, we first consider the 2D case in Figure 1(a). The 2D tensor order parameter is of the form $\mathbf{Q}_{2D} = s(\mathbf{n} \times \mathbf{n} - \mathbf{I}_2/2)$, where $\mathbf{n} \in \mathbf{S}^1$ and $0 \leq s < 1$ [28]. We use the Bingham closure method [29, 30] to define an ODF, $f_{\mathbf{Q}_{2D}}(\mathbf{m})$, for a given \mathbf{Q}_{2D} with $0 \leq s < 1$, where

$$f_{\mathbf{Q}_{2D}}(\mathbf{m}) = \frac{\exp(\mathbf{B}_{\mathbf{Q}_{2D}} : \mathbf{m} \times \mathbf{m})}{\int_{\mathbf{S}^1} \exp(\mathbf{B}_{\mathbf{Q}_{2D}} : \mathbf{m} \times \mathbf{m})}, \quad \mathbf{m} \in \mathbf{S}^1; \quad (5)$$

$\mathbf{B}_{\mathbf{Q}_{2D}}$ is a symmetric traceless 2×2 matrix implicitly determined by \mathbf{Q}_{2D} [31]. Next, we can generate the data and the corresponding label $(\mathbf{Q}_{2D}, f_{\mathbf{Q}_{2D}})$, but it is necessary to convert the label $f_{\mathbf{Q}_{2D}}$ into a finite-dimensional $N \times 1$ vector. One approach is to discretize it into $f_{\mathbf{Q}_{2D}}(\mathbf{m}_j)$, where $\{\mathbf{m}_j\}, 1 \leq j \leq N$, are the discretized points on the unit circle S^1 . However, this would lead to an excessively large number of neurons in the output layer. A more efficient method is to use the discrete spherical harmonics transform [32], \mathbf{A} , which can well approximate $f_{\mathbf{Q}_{2D}}$ with a relatively small N [33]. Further, the spherical harmonics transform is rotationally invariant, that is, if we rotate $f_{\mathbf{Q}_{2D}}(\mathbf{m})$ to $f_{\mathbf{Q}_{2D}}(\mathbf{P}_n \mathbf{m})$, $\mathbf{P}_n \in SO(2)$, then the rotated expansion coefficients can be calculated from $\hat{\mathbf{A}} = \mathbf{R}_n \mathbf{A}$ (see Supplementary Material). Thus, we only sample $\mathbf{Q}_{2D}^i = \text{diag}(s_i/2, -s_i/2)$ for $0 \leq s_i < 1$, with a fixed eigenvector $\mathbf{n}_e = (1, 0)$, and the rest follows from rotational invariance. To maintain frame indifference as in (4), we encode \mathbf{Q}_{2D} as a function of its non-negative eigenvalue $s/2$. We specifically encode \mathbf{Q}_{2D} as s^2 because $s^2 = 2\text{Tr}(\mathbf{Q}_{2D}^2)$ simplifies the differentiation of \mathbf{Q}_{2D} . After training the NN-Tensor model, we obtain the following bulk energy:

$$E_{net}(\mathbf{Q}_{2D}) = E_M(f(\hat{\mathbf{A}}_\theta(s^2))), s^2 = 2\text{Tr}(\mathbf{Q}_{2D}^2), \quad (6)$$

where θ denotes the set of parameters in the neural network and E_M is the molecular free energy in (1).

For 3D NN-Tensor model, the number of 3D discrete spherical harmonics coefficients is much larger than in the 2D case, which results in an excessive number of neurons in the output layer. Therefore, we replace fitting the map between \mathbf{Q} and $f_{\mathbf{Q}}$ with directly labeling \mathbf{Q} by $E_{entropy}(f_{\mathbf{Q}})$ and $E_{potential}(f_{\mathbf{Q}})$ respectively (see Supplementary Material). We ensure frame indifference by encoding \mathbf{Q} as a function of its minimum eigenvalue, λ_1 , and second minimum eigenvalue, λ_2 . Specifically, we encode \mathbf{Q} as $\sum_{i=1}^3 \lambda_i^2 = \text{Tr}(\mathbf{Q}^2)$ and $\sum_{i=1}^3 \lambda_i^3 = \text{Tr}(\mathbf{Q}^3)$ for convenient differentiation, and they are bijective with respect to λ_1 and λ_2 within the domain of definition specified in (3). The 3D NN-Tensor model can be trained to yield the following bulk energy as a function of 3D \mathbf{Q} tensor defined in (2):

$$E_{net}(\mathbf{Q}) = E_M \left(\text{Net}_\theta \left(\sum_{i=1}^3 \lambda_i^2, \sum_{i=1}^3 \lambda_i^3 \right) \right). \quad (7)$$

Phase transitions—We first investigate whether the trained bulk energies in (6) and (7) can accurately capture the I-N phase transition. In the 2D case, we plot

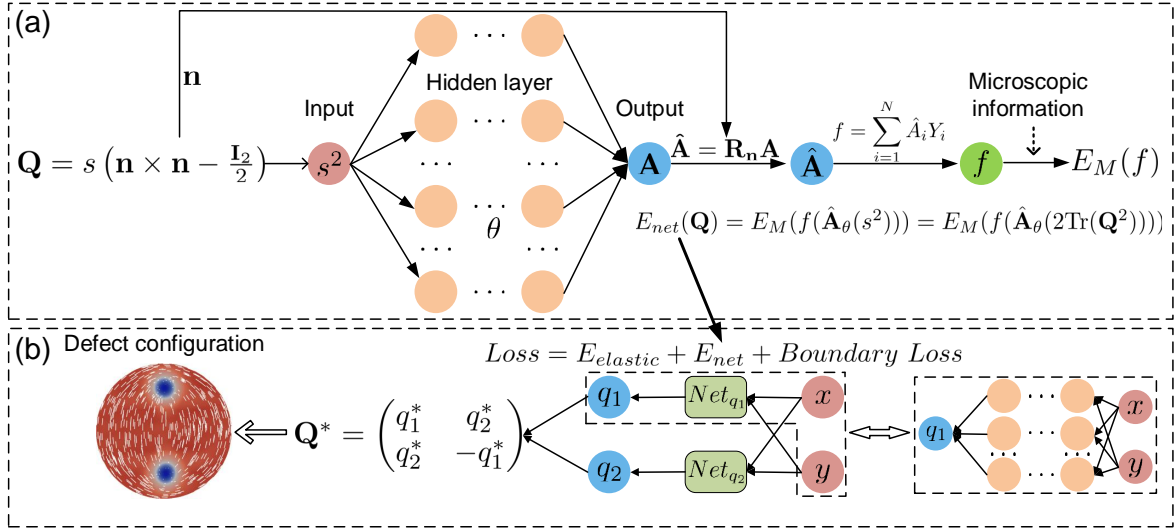


FIG. 1: (a) The 2D NN-Tensor model with microscopic information. The parameters that need to be trained are represented by θ . The 3D NN-Tensor model can be seen in Supplementary Material. (b) The NN-Tensor model is embedded in the loss function of the second neural network to find the stable configurations.

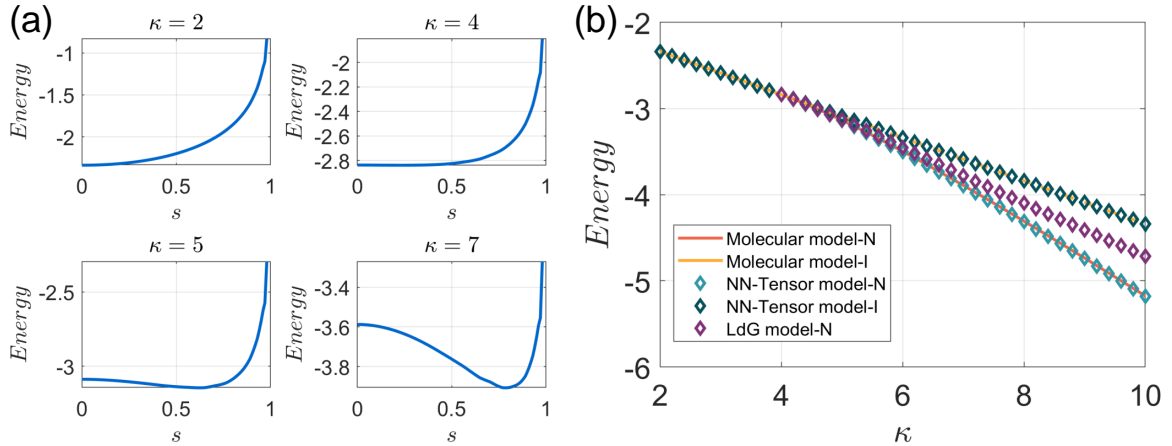


FIG. 2: (a) $E_{net}(\mathbf{Q}_{2D}) = E_M(f(\hat{\mathbf{A}}_\theta(s^2)))$ versus s at $\kappa = 2, 4, 5, 7$. (b) The energies of the isotropic (I) and nematic (N) phases versus κ . The energy of isotropic phase in the NN-Tensor model and molecular model are $E_{net}(\mathbf{Q} = 0)$ and $E_M(f \equiv 1/2\pi)$, respectively. For $\kappa > 4$, the energy of the nematic phase in the NN-Tensor model is $\min_{0 \leq s < 1} E_M(f(\hat{\mathbf{A}}_\theta(s^2)))$, and in the molecular model, it can be analytically calculated [12].

the energy $E_{net}(\mathbf{Q}_{2D})$ in (6) versus s for various values of κ in Figure 2(a). For $\kappa = 2$, the temperature is high and the entropy energy in (1) dominates, so that the isotropic phase $s = 0$ ($\mathbf{Q} = 0$) is the global energy minimizer. For $\kappa = 4$, the isotropic phase nearly loses its stability, which is consistent with the fact that molecular free energy in (1) undergoes a second-order I-N phase transition at $\kappa^* = 4$ [12]. For $\kappa = 5$, the isotropic phase loses stability and the nematic phase with $s \approx 0.64$ achieves the energy minimum. As κ further increases to

7, the nematic phase with $s \approx 0.79$ achieves the energy minimum, indicating that the nematic phase becomes increasingly orientationally ordered as the temperature further decreases. In Figure 2(b), we plot the energies of the isotropic and nematic phases with $E_{net}(\mathbf{Q}_{2D})$ and the M-S free energy (1), demonstrating excellent agreement between the two approaches. In contrast, the LdG model is only accurate near κ^* and fails to provide an accurate approximation at low temperatures.

In the 3D case, we plot the energy in (7) versus λ_1, λ_2 ,

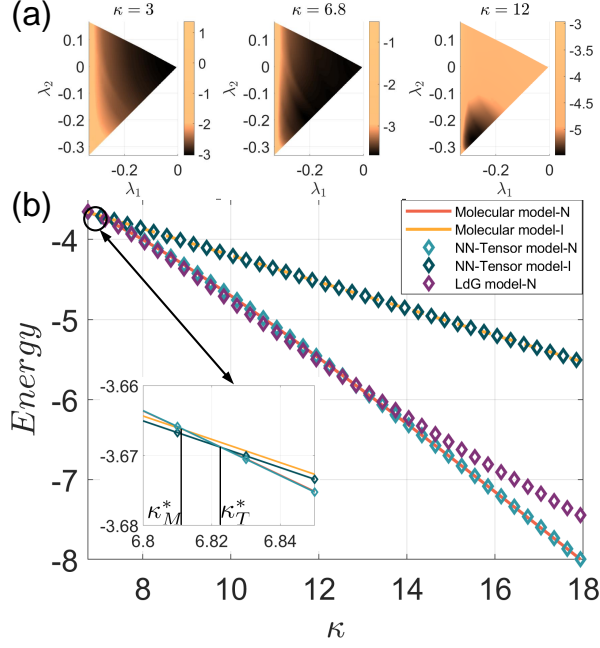


FIG. 3: (a) $E_{net}(\mathbf{Q})$ versus λ_1, λ_2 at $\kappa = 3, 6.8, 12$. (b) The energies of isotropic and nematic phases in the molecular model and NN-Tensor model versus κ . κ_M^* and κ_T^* are the I-N phase transition temperatures in the molecular model and NN-Tensor model, respectively.

for different values of κ in Figure 3(a). For $\kappa = 3$, the isotropic phase $\mathbf{Q} = 0$ ($\lambda_1 = \lambda_2 = 0$) is the global minimizer. At $\kappa = 12$, the isotropic phase loses stability and the nematic phase with $\lambda_1 = \lambda_2 \approx -0.28$ achieves the energy minimum. At $\kappa = 6.8$, there are two energy minimizers: the isotropic phase and the nematic phase (with $\lambda_1 = \lambda_2 \approx -0.132$). Hence, the 3D NN-Tensor model predicts a first-order I-N phase transition, consistent with the molecular model which predicts a first-order I-N phase transition for $\kappa^* \in (6.7, 7.5)$ [9, 12]. In Figure 3(b), the NN-Tensor model fits the molecular model well both near the phase transition temperature, κ_M^* , and for lower temperatures.

Confined NLC systems—For confined spatially inhomogeneous systems, we add a one-constant elastic energy density [18] to the trained bulk energy density to define a total free energy, as shown below:

$$E(\mathbf{Q}) = \int_{\Omega} \frac{1}{2} |\nabla \mathbf{Q}|^2 + \lambda^2 E_{net}(\mathbf{Q}) d\mathbf{x}, \quad (8)$$

where Ω is the rescaled 2D or 3D domain and λ is a scaling parameter that contains information about the geometrical size and macroscopic material properties. In particular, λ is proportional to domain size and large values of λ are experimentally relevant [34, 35]. The physically observable configurations are modelled by energy minimizers subject to the imposed boundary conditions. The end-to-end representation of the bulk energy

density, $E_{net}(\mathbf{Q})$ is convenient for taking the derivative with respect to \mathbf{Q} , which in turn, allows us to find energy minimizers using the gradient descent method. For computational efficiency and flexibility, we use two (five) neural networks, Net_{q_i} , to approximate two (five) elements of the 2D (3D) \mathbf{Q} -tensor (see Figure 1(b)). Numerical tests in the Supplementary Material demonstrate that it reaches minima of (8) faster than classical numerical methods, such as finite difference methods. This neural network approach is domain-free and mesh-free, making it particularly suitable for complex and experimentally relevant domains [36–38]. The minimizer of (8), $\mathbf{Q}_{\theta^*}(x, y)$, is obtained by training Net_{q_i} with the following loss function,

$$\begin{aligned} Loss(\theta) = & \underbrace{\frac{W}{N_b} \sum_{i=1}^{N_b} |\mathbf{Q}_{\theta}(x_i^b, y_i^b) - \mathbf{Q}_{bc}(x_i^b, y_i^b)|^2}_{\text{Boundary Loss}} + \\ & \underbrace{\frac{1}{2N_{in}} \sum_{i=1}^{N_{in}} |\nabla \mathbf{Q}_{\theta}(x_i^{in}, y_i^{in})|^2}_{\text{Elastic}} + \underbrace{\frac{\lambda^2}{N_{in}} \sum_{i=1}^{N_{in}} E_{net}(\mathbf{Q}_{\theta}(x_i^{in}, y_i^{in}))}_{E_b = \lambda^2 E_{net}}, \end{aligned} \quad (9)$$

where $(x_i^{in}, y_i^{in}) \in \Omega \setminus \partial\Omega, i = 1, \dots, N_{in}$ are uniformly sampled points in Ω , and $(x_i^b, y_i^b) \in \partial\Omega, i = 1, \dots, N_b$ are uniformly sampled points on $\partial\Omega$. The boundary loss with penalty weight, W , enforces preferred boundary conditions, represented by \mathbf{Q}_{bc} . Examples of preferred boundary conditions include 2D tangential boundary conditions, $\mathbf{Q}_{bc}(x_i^b, y_i^b) = -s_+(\vec{v}_i^b \times \vec{v}_i^b - \mathbf{I}_2/2)$, and 2D homeotropic boundary conditions, $\mathbf{Q}_{bc}(x_i^b, y_i^b) = s_+(\vec{v}_i^b \times \vec{v}_i^b - \mathbf{I}_2/2)$, where \vec{v}_i^b is the outer normal vector of $\partial\Omega$ at (x_i^b, y_i^b) and the positive constant s_+ measures the degree of orientational ordering at the boundary [14, 34]. In 3D regions, the boundary loss function associated with tangential boundary conditions is given by

$$W \sum_{i=1}^{N_b} \left\| \mathbf{Q}(x_i^b, y_i^b) \vec{v}_i^b + \frac{s_+}{3} \vec{v}_i^b \right\|_2^2. \quad (10)$$

The boundary loss (10) vanishes if and only if the leading eigenvector of \mathbf{Q} lies within and is free to rotate in the tangential plane of $\partial\Omega$. The 3D homeotropic boundary conditions are $\mathbf{Q}_{bc}(x_i^b, y_i^b) = s_+(\vec{v}_i^b \times \vec{v}_i^b - \frac{\mathbf{I}_3}{3})$.

In [39, 40], the authors study NLC systems within regular K polygons, in the 2D LdG framework, with tangent boundary conditions. In [39], a 2D planar bistable nematic device is experimentally manufactured using quasi-2D square wells. For small λ , the LdG theory predicts a unique energy minimizer with an isolated defect (isotropic point) at the polygon centre, referred to as the Ring Solution [40]. For large λ , the LdG systems have $[K/2]$ classes of distinct energy minimizers with a pair of defects pinned at the vertices for a K -regular polygon [40]. The defects migrate to the interior as $K \rightarrow \infty$ and the K -polygon approaches a disc [15]. In Figure 4(a), we

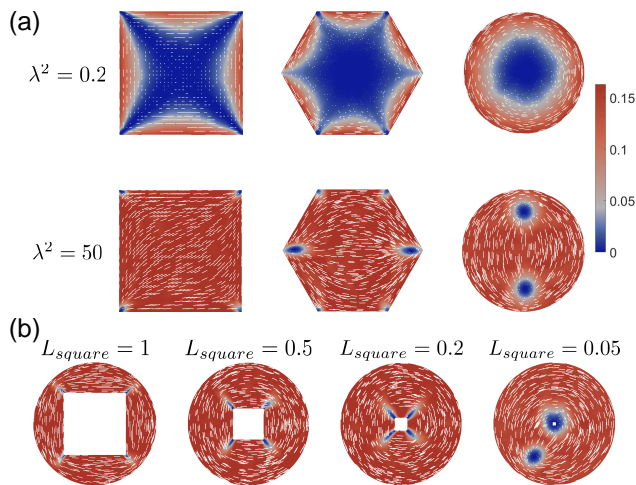


FIG. 4: (a) NN-Tensor model applied to polygons for $\kappa = 7.243$. The defects are the isotropic blue regions. (b) NN-Tensor model applied to a square-holed disc for $\lambda^2 = 50, \kappa = 7.243$. L_{square} is the edge length of the inner square. The color bar labels $q_1^2 + q_2^2 = s^2/4$, and the white lines correspond to the nematic director, defined by the leading eigenvector of \mathbf{Q} .

use the 2D NN-Tensor model to compute energy minimizers of (8) on a square domain, hexagon and disc, for two representative values of λ^2 , and the results are in agreement with the predictions in [15, 39, 40].

In Figure 4(b), we apply the NN-Tensor model to a non-regular domain: square-holed discs, where the rescaled edge length of the inner square is L_{square} . For a large hole with $L_{square} = 1$, four point defects are pinned at the corners. As L_{square} decreases, these four point defects merge and eventually separate into two $+1/2$ point defects. Notably, one point defect is pinned near the hole, indicating that holes can control defect locations. Similar phenomena are also found in self-assembly mechanisms in nematic emulsions [41, 42].

In [43], we study NLC configurations within 3D cuboids, with tangent boundary conditions, in the 3D LdG framework. For shallow cuboids, the minimizer is an almost z -invariant Diagonal (D) state which is consistent with the experimental observation in [39] i.e. the nematic director aligns along one of the square diagonals on the bottom cross-section and this profile is z -invariant along the height of the cuboid. For the cube, the LdG minimizer has a D-type profiles on all six faces, with defects at the corners. In Figure 5 (a-b), we apply the 3D NN-Tensor model to the same problem and recover the LdG and experimental predictions.

We next consider a 3D ball with homeotropic boundary conditions, a very well-studied problem in the LdG framework. We apply the 3D NN-Tensor model to this problem and recover the celebrated radial hedgehog solution with a central point defect, and the biaxial torus solution with a ring disclination, for various domain sizes

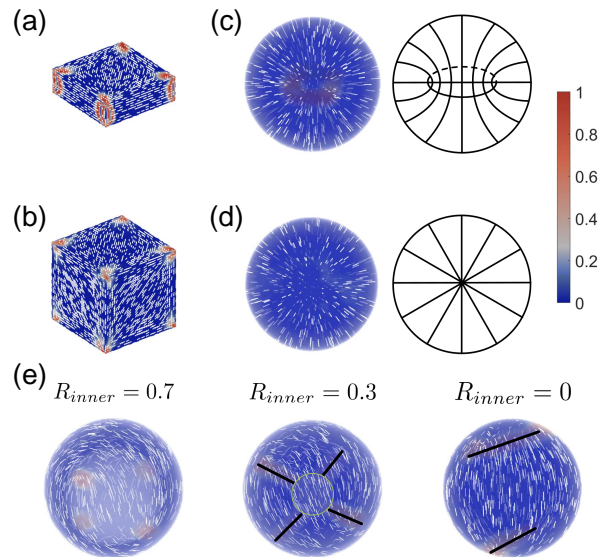


FIG. 5: (a-b) NN-Tensor model applied to cuboids for $\lambda^2 = 50, \kappa = 12$ with $h = 0.3$ and $h = 1$, respectively. (c-d) NN-Tensor model applied to 3D balls with homeotropic boundary conditions, for $\lambda^2 = 30, \kappa = 12$ and $\lambda^2 = 1, \kappa = 12$, respectively. (e) NN-Tensor model applied to two asymmetric shells for $\lambda^2 = 30, \kappa = 12$ with $R_{inner} = 0.7, 0.3, 0$, respectively. The color bar labels the biaxial parameter $\beta(\mathbf{Q}) = 1 - 6 \frac{(\text{Tr}(\mathbf{Q}^3))^2}{(\text{Tr}(\mathbf{Q}^2))^3}$.

as in [44] and [15]. Finally, in Figure 5(e), we consider a more complex 3D region between two asymmetric shells, with tangential boundary conditions in (10), akin to the experimental settings in [37, 38, 45]. We fix the radius of the outer spherical shell, $R_{outer} = 1$, with its center at $(0, 0, 0)$, and place the center of the inner spherical shell at $(0, 0, -0.1)$. We then vary the radius of the inner spherical shell, R_{inner} . With a relatively thin shell, four $+1/2$ defects are experimentally observed [37, 45], which is predicted by our 3D NN-Tensor model at $R_{inner} = 0.7$. For $R_{inner} = 0$, the minimizer of (8) has four point defects on the surface. These point defects are at the endpoints of two non-intersecting $1/2$ disclination lines. For $R_{inner} = 0.3$, the minimizer of (8) exhibits four disclination lines connecting the inner and outer surfaces, demonstrating the crucial role of inner voids in controlling the locations and multiplicity of defects.

In conclusion, we have formulated a computationally efficient NN-Tensor model for NLCs, utilizing a neural network to map the macroscopic \mathbf{Q} -tensor to the microscopic M-S energy. As a result, the NN-Tensor model achieves energy precision comparable to the molecular model, accurately captures the I-N phase transition, and incorporates physical parameters derived directly from molecular information—capabilities beyond the conventional LdG tensor model. We further embed the NN-Tensor model into the loss function of the second neural

network, and stable NLC configurations are obtained by training this neural network in a domain-free and mesh-free manner, making it particularly suitable for complex domains of experimental interest.

We use the NN-Tensor model to represent the bulk energy alone, because the elastic energy is derived analytically in [19]. It should be noted that the NN-Tensor model can be extended to represent the elastic energy too. Furthermore, the NN-Tensor scheme is highly flex-

ible and can be applied to other LC phases, such as the smectic phase [19, 20], to other molecular shapes like bent-core molecules [21] and to other physical systems described by the Landau theory of phase transitions, such as magnetic materials and superconductors [46].

We thank Prof. Patrick E. Farrell for helpful discussions. This work is supported by the National Natural Science Foundation of China (No. 12225102, T2321001, and 12288101) and the Royal Society Newton Advanced Fellowship NAF/R1/180178 awarded to AM and LZ.

-
- [1] P. G. De Gennes and J. Prost, *The physics of liquid crystals*, 83 (Oxford University Press, 1993).
- [2] A. A. Sonin, *Liquid Crystals Reviews* **6**, 109 (2018).
- [3] I. W. Stewart, *The static and dynamic continuum theory of liquid crystals: a mathematical introduction* (Crc Press, 2019).
- [4] J. P. F. Lagerwall and G. Scalia, *Current Applied Physics* **12**, 1387 (2012).
- [5] H. K. Bisoyi and Q. Li, *Chemical Reviews* **122**, 4887 (2021).
- [6] C. Loussert, U. Delabre, and E. Brasselet, *Physical Review Letters* **111**, 037802 (2013).
- [7] W. Wang, L. Zhang, and P. Zhang, *Acta Numerica* **30**, 765 (2021).
- [8] M. Doi and S. F. Edwards, *The theory of polymer dynamics*, Vol. 73 (Oxford University Press, 1988).
- [9] J. Yin, L. Zhang, and P. Zhang, *Physica D* **430**, 133081 (2022).
- [10] W. Y. Zhang, Y. Jiang, and J. Z. Chen, *Physical Review Letters* **108**, 057801 (2012).
- [11] Q. Liang, S. Ye, P. Zhang, and J. Z. Chen, *The Journal of Chemical Physics* **141**, 244901 (2014).
- [12] H. Liu, H. Zhang, and P. Zhang, *Communications in Mathematical Sciences* **3**, 201 (2005).
- [13] S. Wu, J. Wu, H. Cao, Y. Lu, and W. Hu, *Physical Review Letters* **130**, 078101 (2023).
- [14] J. Yin, Y. Wang, J. Z. Chen, P. Zhang, and L. Zhang, *Physical Review Letters* **124**, 090601 (2020).
- [15] Y. Hu, Y. Qu, and P. Zhang, *Communications in Computational Physics* **19**, 354 (2016).
- [16] I. Muševič, M. Škarabot, U. Tkalec, M. Ravnik, and S. Žumer, *Science* **313**, 954 (2006).
- [17] B. Shi, Y. Han, and L. Zhang, *SIAM Journal on Applied Mathematics* **82**, 1808 (2022).
- [18] J. M. Ball and A. Majumdar, *Molecular crystals and liquid crystals* **525**, 1 (2010).
- [19] J. Han, Y. Luo, W. Wang, P. Zhang, and Z. Zhang, *Archive for Rational Mechanics and Analysis* **215**, 741 (2015).
- [20] S. Mei and P. Zhang, *Multiscale Modeling & Simulation* **13**, 977 (2015).
- [21] J. Xu, F. Ye, and P. Zhang, *Multiscale Modeling & Simulation* **16**, 1581 (2018).
- [22] J. Xu, *Physica D: Nonlinear Phenomena* **435**, 133308 (2022).
- [23] J. Behler and M. Parrinello, *Physical Review Letters* **98**, 146401 (2007).
- [24] L. Zhang, J. Han, H. Wang, R. Car, and W. E, *Physical Review Letters* **120**, 143001 (2018).
- [25] L. Zhang, H. Wang, R. Car, and W. E, *Physical Review Letters* **126**, 236001 (2021).
- [26] L. Onsager, *Annals of the New York Academy of Sciences* **51**, 627 (1949).
- [27] W. Maier and A. Saupe, *Zeitschrift für Naturforschung A* **13**, 564 (1958).
- [28] Y. Han, Y. Hu, P. Zhang, and L. Zhang, *Journal of Computational Physics* **396**, 1 (2019).
- [29] C. V. Chaubal, L. G. Leal, and G. H. Fredrickson, *Journal of Rheology* **39**, 73 (1995).
- [30] C. V. Chaubal and L. G. Leal, *Journal of Rheology* **42**, 177 (1998).
- [31] S. Li, W. Wang, and P. Zhang, *Discrete and Continuous Dynamical Systems-B* **20**, 2611 (2015).
- [32] M. J. Mohlenkamp, *Journal of Fourier analysis and applications* **5**, 159 (1999).
- [33] J. Shen, T. Tang, and L.-L. Wang, *Spectral methods: algorithms, analysis and applications*, Vol. 41 (Springer Science & Business Media, 2011).
- [34] G. Canevari, A. Majumdar, and A. Spicer, *SIAM Journal on Applied Mathematics* **77**, 267 (2017).
- [35] B. Shi, Y. Han, J. Yin, A. Majumdar, and L. Zhang, *Nonlinearity* **36**, 2631 (2023).
- [36] P. A. Monderkamp, R. Wittmann, L. B. Cortes, D. G. Aarts, F. Smalenburg, and H. Löwen, *Physical Review Letters* **127**, 198001 (2021).
- [37] H. L. Liang, S. Schymura, P. Rudquist, and J. Lagerwall, *Physical Review Letters* **106**, 247801 (2011).
- [38] J. Noh, Y. Wang, H. L. Liang, V. S. R. Jampani, A. Majumdar, and J. P. Lagerwall, *Physical Review Research* **2**, 033160 (2020).
- [39] C. Tsakonas, A. Davidson, C. Brown, and N. J. Mottram, *Applied physics letters* **90**, 111913 (2007).
- [40] Y. Han, A. Majumdar, and L. Zhang, *SIAM Journal on Applied Mathematics* **80**, 1678 (2020).
- [41] Y. Zhou, B. Senyuk, R. Zhang, I. I. Smalyukh, and J. J. de Pablo, *Nature communications* **10**, 1000 (2019).
- [42] B. Senyuk, A. Mozaffari, K. Crust, R. Zhang, J. J. de Pablo, and I. I. Smalyukh, *Science Advances* **7**, eabg0377 (2021).
- [43] B. Shi, Y. Han, A. Majumdar, and L. Zhang, *SIAM Journal on Applied Mathematics* **84**, 756 (2024).
- [44] S. Mkaddem and E. Gartland Jr, *Physical Review E* **62**, 6694 (2000).
- [45] T. Lopez-Leon, A. Fernandez-Nieves, M. Nobili, and C. Blanc, *Physical Review Letters* **106**, 247802 (2011).
- [46] P. C. Hohenberg and A. P. Krekhov, *Physics Reports* **572**, 1 (2015).